

Geophysical Research Letters[®]



RESEARCH LETTER

10.1029/2022GL100400

Key Points:

- Using multipoint data from Magnetospheric Multiscale, we find that electron heating takes place on ion scales in the quasi-perpendicular shock ramp
- We show that the time series of the temperature does not represent the spatial profile due to varying shock ramp speed
- Electron distributions in the ramp and downstream of the shock show that electrons are heated non-adiabatically

Supporting Information:

Supporting Information may be found in the online version of this article.

Correspondence to:

A. Johlander and A. P. Dimmock,
andreasj@irfu.se;
andrew.dimmock@irfu.se

Citation:

Johlander, A., Khotyaintsev, Y. V., Dimmock, A. P., Graham, D. B., & Lalti, A. (2023). Electron heating scales in collisionless shocks measured by MMS. *Geophysical Research Letters*, 50, e2022GL100400. <https://doi.org/10.1029/2022GL100400>

Received 29 JUL 2022

Accepted 18 JAN 2023

Electron Heating Scales in Collisionless Shocks Measured by MMS

Andreas Johlander¹ , Yuri V. Khotyaintsev¹ , Andrew P. Dimmock¹ , Daniel B. Graham¹ , and Ahmad Lalti^{1,2} 

¹Swedish Institute of Space Physics, Uppsala, Sweden, ²Space and Plasma Physics, Department of Physics and Astronomy, Uppsala University, Uppsala, Sweden

Abstract Electron heating at collisionless shocks in space is a combination of adiabatic heating due to large-scale electric and magnetic fields and non-adiabatic scattering by high-frequency fluctuations. The scales at which heating happens hints to what physical processes are taking place. In this letter, we study electron heating scales with data from the Magnetospheric Multiscale (MMS) spacecraft at Earth's quasi-perpendicular bow shock. We utilize the tight tetrahedron formation and high-resolution plasma measurements of MMS to directly measure the electron temperature gradient. From this, we reconstruct the electron temperature profile inside the shock ramp and find that the electron temperature increase takes place on ion or sub-ion scales. Further, we use Liouville mapping to investigate the electron distributions through the ramp to estimate the deHoffmann-Teller potential and electric field. We find that electron heating is highly non-adiabatic at the high-Mach number shocks studied here.

Plain Language Summary Shock waves appear whenever a supersonic medium, such as a plasma, encounters an obstacle. The plasma, which consists of charged ions and free electrons, is heated by the shock wave through interactions with the electromagnetic fields. In this work, we investigate how electrons are heated at plasma shocks. A key parameter to electron heating is the thickness of the layer where the heating takes place. Here, we use observations from the four Magnetospheric Multiscale spacecraft that regularly cross the standing bow shock that forms when the supersonic plasma, known as the solar wind, encounters Earth's magnetic field. We find that the thickness of the shock is larger than previously reported and is on the scales where ion physics dominate. We also find that the electron heating deviates significantly from simple adiabatic heating.

1. Introduction

Shock waves appear in a wide variety in space plasmas where they act to slow down and heat supersonic flows before the plasma can encounter an obstacle. Plasma shocks in the heliosphere and in astrophysical settings are often collisionless, meaning that heating and entropy generation takes place through interactions between the particles and the electromagnetic fields (Krall, 1997; Parks et al., 2017). Due to the collisionless nature of the shock waves, energy is not partitioned equally between the plasma species. Ions, which gain most of the dissipated energy (e.g., Schwartz et al., 1988; Vink et al., 2015), are principally heated by the instability between gyro-bunched shock-reflected and the transmitted ions (Sckopke et al., 1983).

Electron heating happens in an interplay between the betatron effect through an increase in magnetic field and the electric cross-shock potential (DC fields) on one hand and wave-particle interactions (AC fields) at the shock (Goodrich & Scudder, 1984; Scudder, 1995). Since electron thermal speeds in the solar wind are much greater than the bulk speed, electrons are free to move across the shock along the magnetic field in both directions. The DC fields act to adiabatically inflate the distribution in velocity space, leaving a hole in velocity space. This phase-space inflation is reversible and therefore does not produce entropy (Balikhin et al., 1993; Lindberg et al., 2022). The hole left in velocity is filled by electron scattering by AC fields, which leads to a flat-top electron distribution downstream of the shock (Feldman et al., 1983). Through which processes the non-reversible heating takes place in shocks is not fully understood but short-wavelength electrostatic waves, which likely form from the instability from the inflation of the electron distributions, have been observed at the shock with amplitudes which suggests that they can efficiently scatter electrons (e.g., Bale et al., 1998; Vasko et al., 2018; Vasko et al., 2022).

© 2023. The Authors.

This is an open access article under the terms of the [Creative Commons Attribution License](https://creativecommons.org/licenses/by/4.0/), which permits use, distribution and reproduction in any medium, provided the original work is properly cited.

Table 1
Shock and Upstream Parameters for the Events Studied

Parameter	Event 1	Event 2	Event 3
Date	2015-10-07	2015-12-28	2018-03-17
Time (UTC)	11:37	05:29	22:21
θ_{Bn} [°]	73	51	89
Alfvén Mach number M_A	9	17	10
Fast mode Mach M_f	4	9	6
Electron temp. $T_{e,u}$ [eV]	20	8	11
$T_{e,u}$ measured by Wind [eV]	18	9	12
Max T_e in ramp [eV]	51	56	48
Electron beta $\beta_{e,u}$	2.9	1.9	1.2
Avg. s/c separation $\langle r_{sc} \rangle$ [km]	27	34	25
Ion inertial length $d_{i,u}$ [km]	37	88	90
Electron inertial length $d_{e,u}$ [km]	0.9	2.1	2.1
Electron heating scale [km]	42	69	57

An insight into the electron heating process in the shock can be achieved by measuring the width of the ramp. With multi-spacecraft missions, this is a seemingly straight-forward measurement which has been performed several times. Newbury et al. (1998) used observations by the two ISSE spacecraft and found ramp widths around or below the ion inertial scale and noted the presence of smaller scale structures within the ramp. Bale et al. (2003) on the other hand reported that ramp thickness scales with the gyroradius of shock-reflected ions. Hobara et al. (2010) used observations of the bow shock by the Cluster and THEMIS spacecraft and found that the ramp width is of the order of the ion inertial length and decreases with Mach number. The most detailed investigation of the heating scales to date was done by Schwartz et al. (2011) who used a slow shock crossing observed by Cluster to measure the ramp width using direct measurements of the electron temperature. The authors found that half of the total temperature increase took place on only a few electron inertial lengths, significantly smaller than previously reported.

In this work, we revisit the topic of electron heating scales at collisionless shocks using observations from the Magnetospheric Multiscale (MMS) spacecraft. The combination of the high time-resolution electron observations and the tight tetrahedron formation of MMS allows for a highly accurate and detailed measurement of the electron temperature gradient in three

quasi-perpendicular shock ramps. We further estimate the deHoffmann-Teller potential and reconstruct the electric field in this frame inside the shock ramp and use this to characterize the contributions to electron heating at shocks.

2. Observations

We use observations by the four MMS spacecraft (Burch et al., 2016). Magnetic field data are from the fluxgate magnetometer (Russell et al., 2016) which provides data with a cadence of 128 Hz. Particle data are from the Fast Plasma Investigation (FPI) instrument which measures the electron and ion distributions and moments every 30 and 150 ms, respectively (Pollock et al., 2016). Since FPI is not designed for the cold and fast solar wind, we obtain the proton temperature used to calculate the magnetosonic Mach numbers from Solar Wind Experiment onboard the upstream Wind spacecraft (Ogilvie et al., 1995), time-shifted and obtained from the OMNI database (King & Papitashvili, 2005). We also validate the upstream electron temperature from MMS with Wind measurements using the time-lag given by OMNI, see Table 1.

We select three quasi-perpendicular bow shock crossings from the MMS data from 2015 to 2018 when electron data from FPI onboard all four spacecraft is available. In the selection, we used the following criteria to find suitable events: (a) the shock crossing should be fast, so that time-evolution of the ramp plays a limited role, (b) all four spacecraft should be in the ramp at the same time, and (c) the four-spacecraft measurements in electron temperature should be clearly separated so that the gradient of electron temperature can be measured accurately. This selection resulted in three shock crossings from hundreds of quasi-perpendicular shock crossings available from this time (Lalti et al., 2022) meaning that these criteria are rarely satisfied by MMS at the bow shock due to the typically very small spacecraft separation. This is an early indication that the temperature gradient scales at the shock are larger than the typical MMS separation of 5–30 km.

An overview of one of the elected events, named Event 1, observed by MMS1 is shown in Figure 1. The spacecraft crosses the bow shock from the downstream magnetosheath and into the upstream solar wind. The shock ramp is seen as a sharp boundary in number density N and electron temperatures. The parallel and perpendicular temperatures are similar in the ramp and downstream of the shock with temperature anisotropy close to 1. From now on, we consider the scalar electron temperature $T_e = (2T_{e,\perp} + T_{e,\parallel})/3$. We determine the shock normal of this shock and the other two events by selecting up- and downstream time intervals and using the mixed mode method (Abraham-Shrauner, 1972; Schwartz, 1998). The time intervals used for the normal vectors is found in Table S1 in Supporting Information S1. We find that the shock shown in Figure 1 is quasi-perpendicular with $\theta_{Bn} = 73^\circ$ and moderately high Mach number with $M_A = 9$. These and other shock parameters for all events are listed in

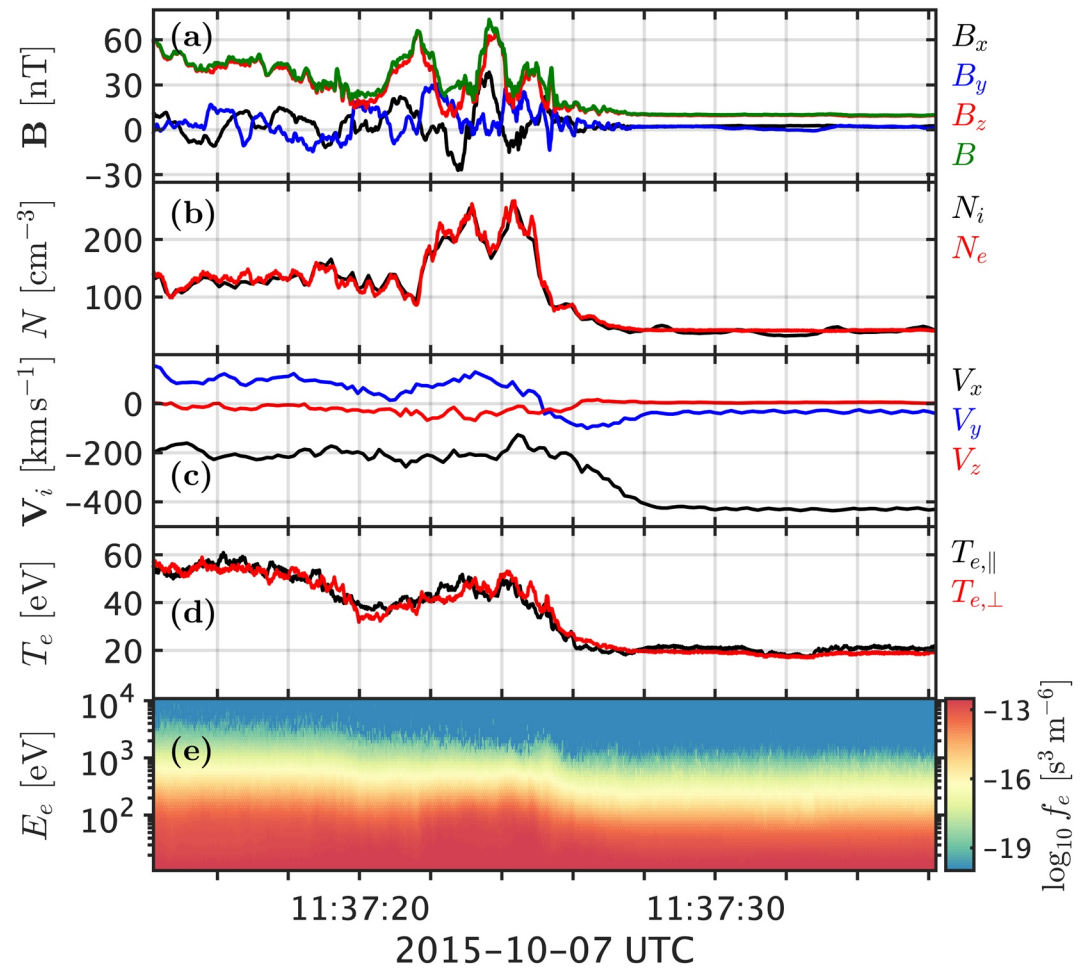


Figure 1. Shock crossing by Magnetospheric Multiscale1. (a) Magnetic field \mathbf{B} in GSE coordinates. (b) Ion and electron number densities $N_{i,e}$. Ion flow velocity \mathbf{V}_i . (c) Ion flow velocity \mathbf{V}_i . (d) Parallel and perpendicular electron temperature $T_{e,\parallel}$ and $T_{e,\perp}$. (e) Omni-directional electron phase-space density as a function of energy.

Table 1. The three selected events are quasi-perpendicular with Alfvén Mach numbers ranging from 9 to 17 which is relatively high compared to most times MMS has encountered the bow shock, cf. (Lalti et al., 2022).

3. Electron Heating Scales

To investigate the electron heating scales we now look at the four-spacecraft observations from the shock crossing, shown in Figure 2. Panel (c) shows the four-spacecraft observations of T_e for Event 1. We can see that the temperature decrease from downstream to upstream takes place in two distinct steps with a plateau between them, similar to previous observations (Schwartz et al., 2011). It is possible to perform a four-spacecraft timing analysis to obtain the shock ramp speed from the temperature measurements. However, this would be sensitive to what parts of the ramp are being used to find the time-shifts, which may indicate that the shock ramp speed is varying even during this fast shock crossing. The apparent change in ramp speed could possibly be due to the shock front appearing to move back and forth as a result of shock ripples (Johlander et al., 2016; Winske & Quest, 1988) or wave steepening (e.g., Dimmock et al., 2019; Krasnoselskikh et al., 2002) causing the gradient scales of the shock to change during the crossing. The varying shock speed could also be due to varying upstream conditions (Maksimovic et al., 2003), although these variations would have to be relatively small-scale.

Considering the apparent changes in the ramp speed, to better reconstruct the true ramp profile, we instead use a modified version of the Spatio-Temporal Difference method developed by Shi et al. (2006) based on previous work on dimensionality of plasma structures (Shi et al., 2005). The original method uses multi-point measurements of the magnetic field vector. With FPI's high cadence plasma measurements onboard MMS, it is possible to extend

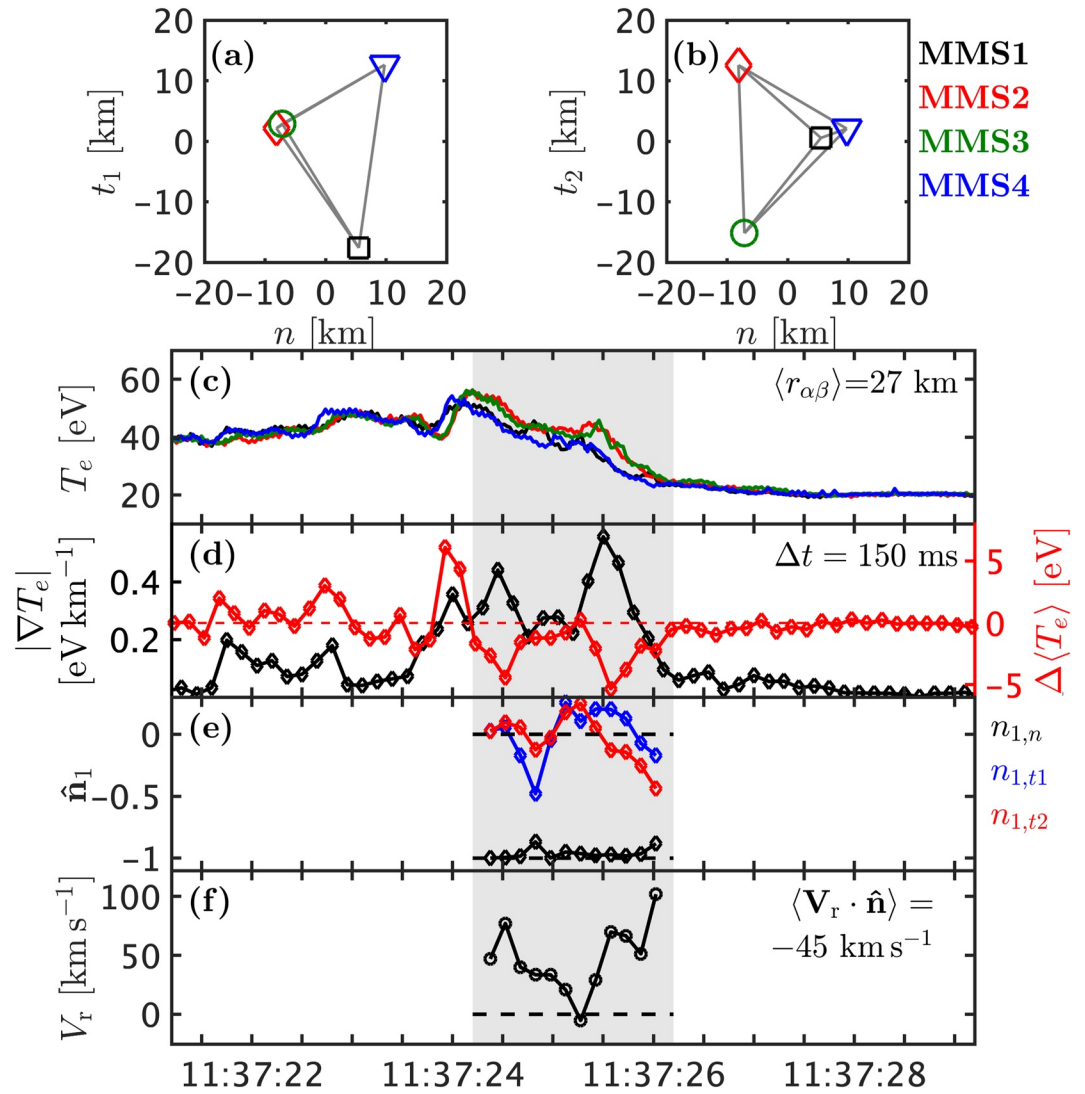


Figure 2. Shock crossing seen by the four spacecraft. (a and b) Relative spacecraft positions in the $n-t_1$ and $n-t_2$ planes. (c) Four-spacecraft measurements of T_e . (d) Left: $|\nabla T_e|$ in black and right: $\Delta \langle T_e \rangle$ in red. (e) Maximum derivative direction \hat{n}_1 . (f) V_r calculated from Equation 2.

this method to plasma quantities such as T_e . Using this quantity, we can, like Schwartz et al. (2011), directly measure the electron heating scales without relying on proxies such as magnetic field or density. The spatio-temporal difference method uses the material derivative of the plasma with the assumption of quasi-stationarity, that is, that local changes are small compared to the convection of the shock (Shi et al., 2006). This means that

$$\frac{dT_e}{dt} = -\mathbf{V}_r \cdot \nabla T_e, \quad (1)$$

where dT_e/dt is the time derivative of the time series of T_e observed by the spacecraft, ∇T_e is the temperature gradient obtained through multi-point measurements (Chanteur, 1998), and \mathbf{V}_r is the instantaneous ramp velocity in the spacecraft frame of reference. Unlike in the analysis by Shi et al. (2006), since we use a scalar quantity for the method, it is only possible to obtain the maximum derivative direction which simply takes the form $\hat{n}_1 = \nabla T_e / |\nabla T_e|$ and $\mathbf{V}_r = V_r \hat{n}_1$. We then obtain the ramp speed

$$V_r = -\frac{\Delta \langle T_e \rangle}{\Delta t |\nabla T_e|}, \quad (2)$$

where $\Delta \langle T_e \rangle$ is the change of the four-spacecraft average of T_e and Δt is the time step between measurements.

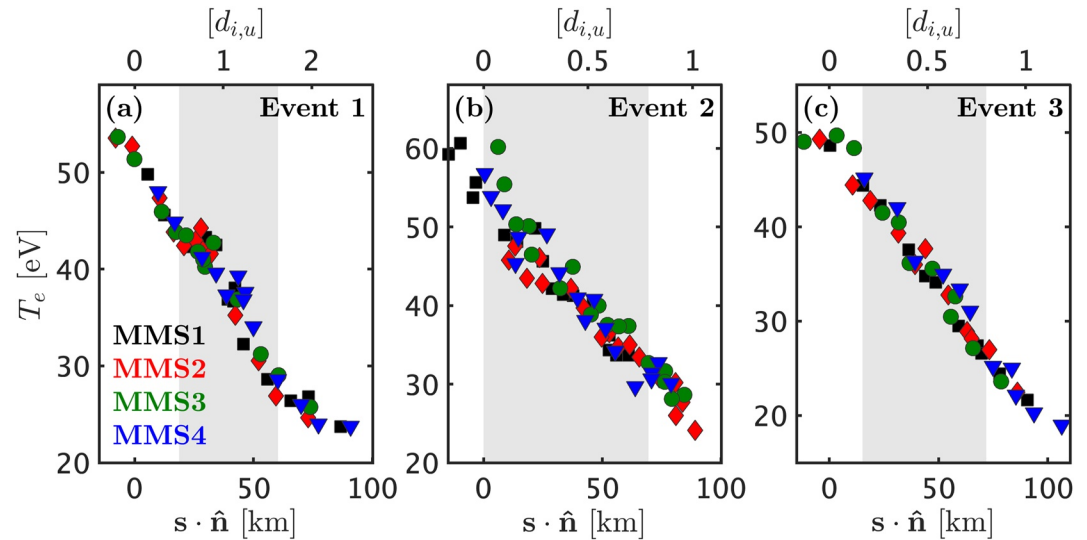


Figure 3. Electron temperature profiles for the three shock crossing events. The x -axes show the profile along \hat{n} which means that upstream is at higher values regardless of which direction the spacecraft crossed the shock. Units are km on the bottom and $d_{i,u}$ on the top. The shortest distance where half the temperature increase takes place is marked in gray.

The method to obtain the ramp speed is illustrated in Figure 2. The spacecraft were at the time of the crossing in a tetrahedron formation with average inter-spacecraft distance of 27 km. Figure 2d shows the terms used in Equation 2. To avoid the influence of small-scale fluctuations and noise in T_e and at the same time fulfill $\langle r_{\alpha\beta} \rangle \gg V_r \Delta t$ (Shi et al., 2006), the electron data here are downsampled to 150 ms resolution. The time interval used to obtain the ramp speed is marked in gray. The resulting unit vector \hat{n}_1 is rotated into a Cartesian coordinate system aligned with the shock and the magnetic field, where \hat{n} is the shock normal, \hat{t}_1 lies in the coplanarity plane, and \hat{t}_2 is out-of-plane, see (e.g., Johlander et al., 2018). We see in panel (e) that ∇T_e and \hat{n}_1 are essentially anti-parallel to \hat{n} throughout the ramp interval and deviates at most 30° from this direction. The resulting ramp speed along \hat{n}_1 is shown in Figure 2f and, supporting our initial suspicion, does vary during the crossing. The ramp speed starts out at $\sim 50 \text{ km s}^{-1}$ and goes to zero and then back up, corresponding to the two jumps and the plateau in T_e profile. The mean ramp speed along \hat{n} in this case is -45 km s^{-1} which is slightly lower than the speed obtained from four-spacecraft timing of $-59 \pm 7 \text{ km s}^{-1}$ (Vogt et al., 2011).

The next step is to obtain the electron heating scale of the shock. To obtain the shock ramp temperature profile, we integrate \mathbf{V}_r over time to obtain the spacecraft position \mathbf{s} relative to the shock. The temperature profiles along \hat{n} for Event 1 are shown in Figure 3a. We can see that the temperature change takes place over nearly 100 km, which is larger than the upstream ion inertial length and significantly larger than reported by Schwartz et al. (2011). We can also see that the plateau seen in T_e in the time series in Figure 2c is not present in the spatial profile due to the decrease in \mathbf{V}_r in the middle of the ramp. This highlights the fact that spacecraft time series observations do not always correspond to spatial profiles at nonstationary or evolving shocks.

We repeat the calculations above for the other two events. Figure 3 shows the spatial profile of T_e for the three events. Figures showing the calculation of \mathbf{V}_r for these events can be found in Figures S1 and S2 in Supporting Information S1. Events 2 and 3 show similar spatial profiles with heating scales comparable to the upstream ion inertial length $d_{i,u}$. To compare to the results by Schwartz et al. (2011), we define the *electron heating scale* as the shortest distance where half the temperature increase between $T_{e,u}$ and the maximum T_e in the selected ramp interval. These distances are shaded with gray in Figure 3 and the scales are listed in Table 1. We see that for these three events, the electron heating scales are $\sim 0.5 - 1 d_{i,u}$, which is similar to that found by Hobara et al. (2010), but significantly larger than the results by Schwartz et al. (2011). These electron heating scales are also significantly smaller than the density gradient scales reported by Bale et al. (2003).

We conclude this section with a short discussion on the results. Here, we select three shock crossings by MMS. In the selection, we have gone through hundreds of shocks crossings in search for suitable candidates. The inter-spacecraft separation of MMS during the time we investigated is normally 5–30 km at the bow shock, which

means that we clearly have a selection bias toward large spacecraft separations, see Table 1. In fact, when the spacecraft are closer together, the measurements of T_e are too close to accurately determine ∇T_e , which means that it is essentially a single-point measurement. This selection bias in our events could indicate that the heating scales that we obtain should be considered as a lower limit.

4. Cross-Shock Potential

After examining the heating scales, we now take a closer look at how electrons are heated at the three shock crossings. Due to the relatively large heating scales in these events, one could possibly expect that the magnetic moment of the electrons be conserved, at least in the absence of wave-particle interactions (Balikhin et al., 1993). To compare the observed electron distributions to those produced by adiabatic heating, we need to measure the cross-shock potential in the deHoffmann-Teller frame (de Hoffmann & Teller, 1950) ϕ^{HT} . The most reliable way to do this (Schwartz et al., 2021) is to perform a Liouville mapping of the electron distribution.

Liouville-mapping is based on conservation of phase-space density according to the Vlasov equation and allows us to determine the electrostatic potential between upstream plasma and a given point in the shock. We reorder the electron distribution in the spacecraft rest frame to a Cartesian field-aligned velocity grid (v_{\parallel} , v_{\perp}) by interpolating and averaging the 3D measured distribution. We select a time interval in the solar wind and use the average distribution as a reference distribution f_{ref} . We then obtain the Liouville-mapped distribution f_L using the measured B and a guess of ϕ^{HT} using the method described by Lefebvre et al. (2007), which assumes conservation of the magnetic moment and therefore adiabatic electron heating. The mapping is done by assuming gyrotropic distributions and tracing electron trajectories to or from the reference distribution and assuming constant phase-space density along the trajectories. Since we are mainly interested in ϕ^{HT} in the shock ramp, we ignore the effects from the overshoot. Also, unlike Lefebvre et al. (2007), we find the ϕ^{HT} by minimizing a quantity with a similar definition to non-Maxwellianity (Graham et al., 2021) which adopts a value between 0 and 1 and in this coordinate system becomes

$$\epsilon_L = \frac{2\pi}{n_e + n_L} \int |f_e(v_{\parallel}, v_{\perp}) - f_L(v_{\parallel}, v_{\perp})| v_{\perp} dv_{\parallel} dv_{\perp}, \quad (3)$$

where f_e is the measured electron distribution and n_e and n_L are the measured and mapped number density respectively. For this case we limit the calculation of ϵ_L to parts of velocity space where $f_e \in [5 \times 10^{-17}, 5 \times 10^{-15}]$ $\text{s}^3 \text{m}^{-6}$, which is below the solar wind peak f_e and above the noise limit, where the assumption of adiabatic heating can be expected to be fulfilled.

Figure 4 shows the results from the Liouville mapping for Event 1. We see that ϕ^{HT} reaches values of ~ 150 eV, similar to previously reported values at Earth's bow shock (e.g., Lefebvre et al., 2007; Schwartz et al., 2021). Panels (d–f) show electron distributions in the marked times in the downstream, ramp, and solar wind. The regions of velocity space determined by the limits of f_e are shown by gray lines. The multi-point measurements of ϕ^{HT} inside the ramp offer a unique opportunity to directly measure the deHoffmann-Teller electric field in the shock, something that is not possible with electric field instruments (Schwartz et al., 2021). Again, under the assumption of quasi-stationarity, this electric field is simply $\mathbf{E}^{\text{HT}} = -\nabla \phi^{\text{HT}}$. We see that \mathbf{E}^{HT} reconstructed from the cross-shock potential is mainly along $\hat{\mathbf{n}}$ as expected, and reaches a value of ~ 2 mV m^{-1} .

We now look closer at the electron distribution function inside of the shock ramp in Figures 4g–4i. We see the distribution mapped from the solar wind to the ramp in red and the actual measured distribution in black. It is clear that the measured electron distribution is less steep than expected by mapping the solar wind electron distribution to the ramp. At energies below ~ 200 eV, the mapped solar wind distribution in red overestimates the measured distribution in black while the opposite is true at higher energies. This means that the phase-space density along the electron trajectories across the shock is not constant due to some scattering and the electron heating is non-adiabatic. The same trend (not shown) persists throughout the downstream region and shows that electrons undergo strong non-adiabatic heating. The same trend is visible in the other two events studied here, which all have relatively high Mach numbers. However, we find electron distributions in much better agreement with adiabatic heating at low-Mach shocks, see Figure S3 in Supporting Information S1. It is worth noting that the mismatch in slopes in Figures 4g–4i is present in both the parallel and anti-parallel directions, which in this case corresponds to toward upstream and downstream respectively. This indicates that electrons crossing from

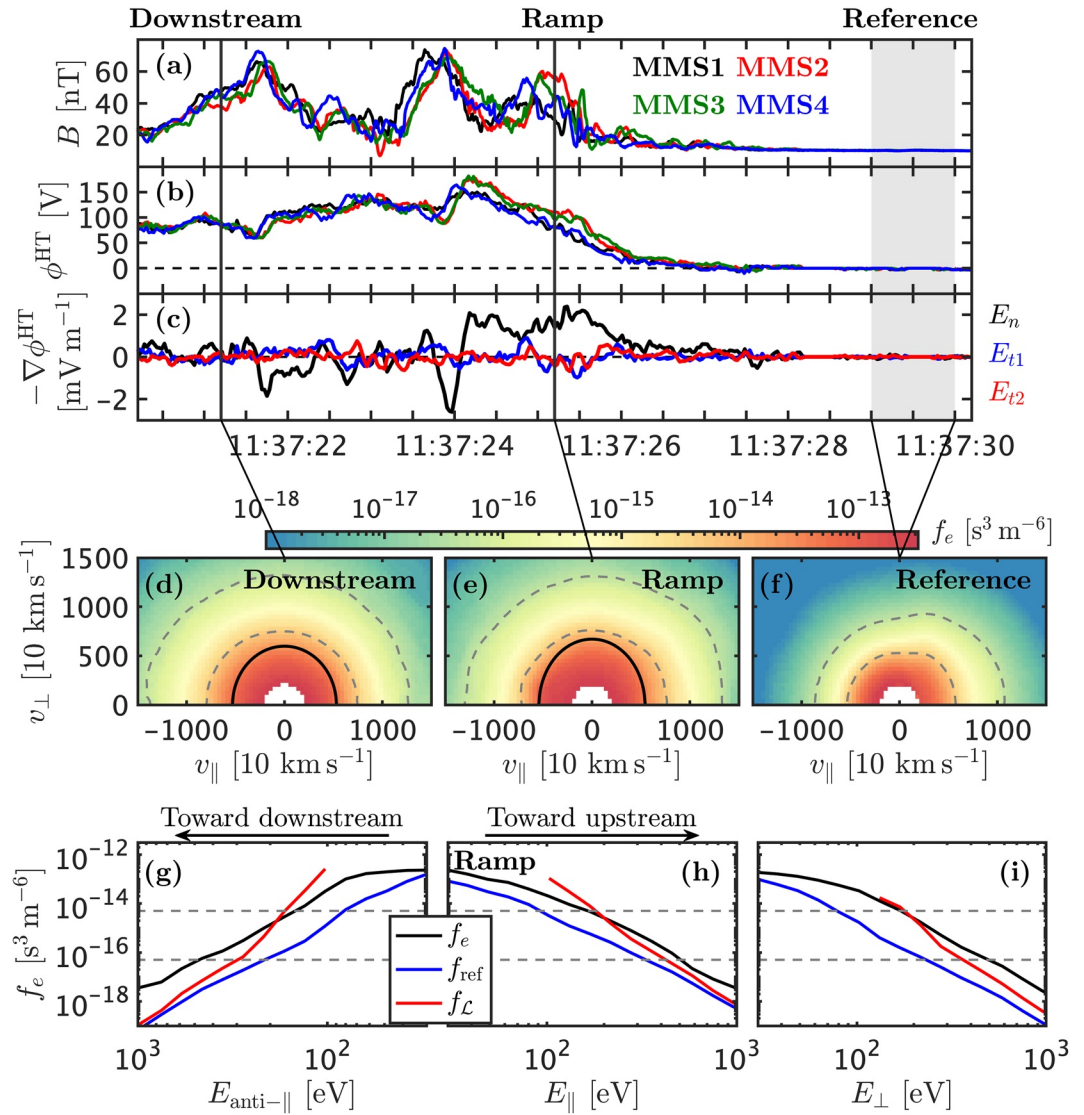


Figure 4. Results from Liouville mapping for the four MMS spacecraft. Time series of: (a) B , (b) ϕ^{HT} , (c) the de Hoffmann-Teller frame electric field from $-\nabla\phi^{\text{HT}}$. Times in the downstream, ramp, and interval for the reference distributions are marked. (d–f) Corresponding electron distributions for the three times measured by MMS1. Mapping limits are shown by gray dashed lines. The solid black lines mark areas where no trajectory can be traced to or from the solar wind. (g)–(i) Line plots showing electron distributions in the (anti-)parallel and perpendicular directions (10° bins) in the shock ramp. Black lines show the measured distribution in the ramp, blue lines are from the solar wind, and red lines are the mapped solar wind distributions.

upstream to downstream are accelerated by some process while electrons crossing in the opposite direction are simultaneously decelerated compared to simple adiabatic heating/cooling.

5. Conclusions

We investigate the scales at which electrons are heated in quasi-perpendicular collisionless shocks. We use MMS observations from three separate encounters with Earth's bow shock and apply the spatio-temporal difference method (Shi et al., 2006) to obtain the spatial electron temperature profiles. Using this method, made possible by MMS's unique capabilities, we provide accurate measurements of the electron heating scales at shocks. We find that half the total temperature increase in the observed shock crossings takes place on ion or sub-ion scales $\sim 0.5 - 1d_{i,u}$, in line with some previous multi-spacecraft measurements (Hobara et al., 2010) but significantly

larger than reported by Schwartz et al. (2011). These results are important for electron acceleration at shock waves in the heliosphere and at astrophysical shocks as an increase in shock thickness can lead to fewer electron scale gradients required for acceleration (Cole, 1976) and lower efficiency of stochastic shock drift acceleration (Amano & Hoshino, 2022; Katou & Amano, 2019).

In one of the studied events, we find that the electron temperature rise from upstream to downstream takes place in two discreet steps with a plateau between them. Multi-spacecraft data reveals that there is still a significant temperature gradient during the plateau, which likely means that the ramp speed is close to zero. Such variation of the ramp speed during the short crossing is possibly due to shock rippling (Johlander et al., 2016) or wave steepening (Krasnoselskikh et al., 2002). Thus using an erroneous assumption of a constant ramp speed will lead to errors in scale estimates, which likely explains the smaller heating scales reported by Schwartz et al. (2011). The actual spatial temperature profile is more monotonic across the shock ramp than can be guessed from the time series of T_e . This highlights the often overlooked fact that time series data not necessarily correspond to spatial profiles at Earth's highly dynamical bow shock.

Last, we investigate how the electrons are heated through the shock ramp and into the downstream. We infer the deHoffmann-Teller cross-shock potential from Liouville mapping (Lefebvre et al., 2007) the high-cadence measured electron distribution functions. Thanks to the multi-point measurements, we can for the first time directly estimate the deHoffmann-Teller electric field inside of the shock ramp and find that its directed along the shock normal and reaches a value of $\sim 2 \text{ mV m}^{-1}$. Furthermore, we find that the electron distributions in the ramp and downstream poorly match the mapped solar wind distribution and do not exhibit the typical flat-top distribution. This means that the electron heating is highly non-adiabatic. We find indications that the electron distribution behave more adiabatically at lower Mach numbers, see Figure S3. Future work should focus on the parametric dependence on electron heating in the shock combined with identifying the processes responsible for scattering and non-reversible heating at the shock.

Data Availability Statement

The Magnetospheric Multiscale (MMS) data are available through the MMS Science Data Center <https://lasp.colorado.edu/mms/sdc/public/>. The OMNI data are available from the GSFC/SPDF OMNIWeb interface <https://omniweb.gsfc.nasa.gov>. The Wind data are available from <https://wind.nasa.gov/> Data analysis was performed using the IRFU-Matlab analysis package.

Acknowledgments

This research was made possible with the data and efforts of the people of the Magnetospheric Multiscale mission. The work was funded by the SHARP project under the European Union's Horizon 2020 research and innovation program with grant agreement number 101004131. APD received financial support from the Swedish National Space Agency (SNSA) Grant 2020-00111, DBG from SNSA Grant 128/17, and AL from the Swedish Research Council Grant 2018-05514.

References

- Abraham-Shrauner, B. (1972). Determination of magnetohydrodynamic shock normals. *Journal of Geophysical Research*, 77(4), 736–739. <https://doi.org/10.1029/JA077i004p00736>
- Amano, T., & Hoshino, M. (2022). Theory of electron injection at oblique shock of finite thickness. *The Astrophysical Journal*, 927(1), 132. <https://doi.org/10.3847/1538-4357/ac4f49>
- Bale, S. D., Kellogg, P. J., Larsen, D. E., Lin, R. P., Goetz, K., & Lepping, R. P. (1998). Bipolar electrostatic structures in the shock transition region: Evidence of electron phase space holes. *Geophysical Research Letters*, 25(15), 2929–2932. <https://doi.org/10.1029/98GL02111>
- Bale, S. D., Mozer, F. S., & Horbury, T. S. (2003). Density-Transition scale at quasiperpendicular collisionless shocks. *Physical Review Letters*, 91(26), 265004. <https://doi.org/10.1103/PhysRevLett.91.265004>
- Balikhin, M., Gedalin, M., & Petrukovich, A. (1993). New mechanism for electron heating in shocks. *Physical Review Letters*, 70(9), 1259–1262. <https://doi.org/10.1103/PhysRevLett.70.1259>
- Burch, J. L., Moore, T. E., Torbert, R. B., & Giles, B. L. (2016). Magnetospheric multiscale overview and science objectives. *Space Science Reviews*, 199(1–4), 5–21. <https://doi.org/10.1007/s11214-015-0164-9>
- Chanteur, G. (1998). Spatial interpolation for four spacecraft: Theory. *ISSI Scientific Reports Series*, 1, 349–370.
- Cole, K. D. (1976). Effects of crossed magnetic and (spatially dependent) electric fields on charged particle motion. *Planetary and Space Science*, 24(5), 515–518. [https://doi.org/10.1016/0032-0633\(76\)90096-9](https://doi.org/10.1016/0032-0633(76)90096-9)
- de Hoffmann, F., & Teller, E. (1950). Magneto-hydrodynamic shocks. *Physics Reviews*, 80(4), 692–703. <https://doi.org/10.1103/PhysRev.80.692>
- Dimmock, A. P., Russell, C. T., Sagdeev, R. Z., Krasnoselskikh, V., Walker, S. N., Carr, C., et al. (2019). Direct evidence of nonstationary collisionless shocks in space plasmas. *Science Advances*, 5(2), eaau9926. <https://doi.org/10.1126/sciadv.aau9926>
- Feldman, W. C., Anderson, R. C., Bame, S. J., Gary, S. P., Gosling, J. T., McComas, D. J., et al. (1983). Electron velocity distributions near the earth's bow shock. *Journal of Geophysical Research*, 88(A1), 96–110. <https://doi.org/10.1029/JA088iA01p00096>
- Goodrich, C. C., & Scudder, J. D. (1984). The adiabatic energy change of plasma electrons and the frame dependence of the cross-shock potential at collisionless magnetosonic shock waves. *Journal of Geophysical Research*, 89(A8), 6654–6662. <https://doi.org/10.1029/JA089iA08p06654>
- Graham, D. B., Khotyaintsev, Y. V., André, M., Vaivads, A., Chasapis, A., Matthaeus, W. H., et al. (2021). Non-maxwellianity of electron distributions near earth's magnetopause. *Journal of Geophysical Research: Space Physics*, 126(10), e2021JA029260. <https://doi.org/10.1029/2021JA029260>

- Hobara, Y., Balikhin, M., Krasnoselskikh, V., Gedalin, M., & Yamagishi, H. (2010). Statistical study of the quasi-perpendicular shock ramp widths. *Journal of Geophysical Research*, 115(A11). <https://doi.org/10.1029/2010JA015659>
- Johlander, A., Schwartz, S. J., Vaivads, A., Khotyaintsev, Y. V., Gingell, I., Peng, I. B., et al. (2016). Rippled quasiperpendicular shock observed by the magnetospheric multiscale spacecraft. *Physical Review Letters*, 117(16), 165101. <https://doi.org/10.1103/PhysRevLett.117.165101>
- Johlander, A., Vaivads, A., Khotyaintsev, Y. V., Gingell, I., Schwartz, S. J., Giles, B. L., et al. (2018). Shock ripples observed by the mms spacecraft: Ion reflection and dispersive properties. *Plasma Physics and Controlled Fusion*, 60(12), 125006. <https://doi.org/10.1088/1361-6587/aae920>
- Katou, T., & Amano, T. (2019). Theory of stochastic shock drift acceleration for electrons in the shock transition region. *The Astrophysical Journal*, 874(2), 119. <https://doi.org/10.3847/1538-4357/ab0d8a>
- King, J. H., & Papitashvili, N. E. (2005). Solar wind spatial scales in and comparisons of hourly Wind and ACE plasma and magnetic field data. *Journal of Geophysical Research (Space Physics)*, 110(A2), A02104. <https://doi.org/10.1029/2004JA010649>
- Krall, N. A. (1997). What do we really know about collisionless shocks? *Advances in Space Research*, 20(4–5), 715–724. [https://doi.org/10.1016/S0273-1177\(97\)00461-4](https://doi.org/10.1016/S0273-1177(97)00461-4)
- Krasnoselskikh, V. V., Lembège, B., Savoini, P., & Lobzin, V. V. (2002). Nonstationarity of strong collisionless quasiperpendicular shocks: Theory and full particle numerical simulations. *Physics of Plasmas*, 9(4), 1192–1209. <https://doi.org/10.1063/1.1457465>
- Lali, A., Khotyaintsev, Y. V., Dimmock, A. P., Johlander, A., Graham, D. B., & Olshevsky, V. (2022). A database of mms bow shock crossings compiled using machine learning. *Journal of Geophysical Research: Space Physics*, 127(8), e2022JA030454. <https://doi.org/10.1029/2022JA030454>
- Lefebvre, B., Schwartz, S. J., Fazakerley, A. F., & Décreau, P. (2007). Electron dynamics and cross-shock potential at the quasi-perpendicular Earth's bow shock. *Journal of Geophysical Research*, 112(A9), A09212. <https://doi.org/10.1029/2007JA012277>
- Lindberg, M., Vaivads, A., Raptis, S., Lindqvist, P.-A., Giles, B. L., & Gershman, D. J. (2022). Electron kinetic entropy across quasi-perpendicular shocks. *Entropy*, 24(6), 745. <https://doi.org/10.3390/e24060745>
- Maksimovic, M., Bale, S. D., Horbury, T. S., & André, M. (2003). Bow shock motions observed with CLUSTER. *Geophysical Research Letters*, 30(7), 1393. <https://doi.org/10.1029/2002GL016761>
- Newbury, J. A., Russell, C. T., & Gedalin, M. (1998). The ramp widths of high-Mach-number, quasi-perpendicular collisionless shocks. *Journal of Geophysical Research*, 103(A12), 29581–29594. <https://doi.org/10.1029/1998JA900024>
- Ogilvie, K. W., Chornay, D. J., Fritzenreiter, R. J., Hunsaker, F., Keller, J., Lobell, J., et al. (1995). SWE, A comprehensive plasma instrument for the wind spacecraft. *Space Science Reviews*, 71(1–4), 55–77. <https://doi.org/10.1007/BF00751326>
- Parks, G. K., Lee, E., Fu, S. Y., Lin, N., Liu, Y., & Yang, Z. W. (2017). Shocks in collisionless plasmas. *Reviews of Modern Plasma Physics*, 1(1), 1. <https://doi.org/10.1007/s41614-017-0003-4>
- Pollock, C., Moore, T., Jacques, A., Burch, J., Gliese, U., Saito, Y., et al. (2016). Fast plasma investigation for magnetospheric multiscale. *Space Science Reviews*, 199(1–4), 331–406. <https://doi.org/10.1007/s11214-016-0245-4>
- Russell, C. T., Anderson, B. J., Baumjohann, W., Bromund, K. R., Dearborn, D., Fischer, D., et al. (2016). The magnetospheric multiscale magnetometers. *Space Science Reviews*, 199(1–4), 189–256. <https://doi.org/10.1007/s11214-014-0057-3>
- Schwartz, S. J. (1998). Shock and discontinuity normals, Mach numbers, and related parameters. *ISSI Scientific Reports Series*, 1, 249–270.
- Schwartz, S. J., Ergun, R., Kucharek, H., Wilson, L., Chen, L.-J., Goodrich, K., et al. (2021). Evaluating the deHoffmann-Teller cross-shock potential at real collisionless shocks. *Journal of Geophysical Research (Space Physics)*, 126(8), e29295. <https://doi.org/10.1029/2021JA029295>
- Schwartz, S. J., Henley, E., Mitchell, J., & Krasnoselskikh, V. (2011). Electron temperature gradient scale at collisionless shocks. *Physical Review Letters*, 107(21), 215002. <https://doi.org/10.1103/PhysRevLett.107.215002>
- Schwartz, S. J., Thomsen, M. F., Bame, S. J., & Stansberry, J. (1988). Electron heating and the potential jump across fast mode shocks. *Journal of Geophysical Research*, 93(A11), 12923–12931. <https://doi.org/10.1029/JA093iA11p12923>
- Scokopke, N., Paschmann, G., Bame, S. J., Gosling, J. T., & Russell, C. T. (1983). Evolution of ion distributions across the nearly perpendicular bow shock: Specularly and non-specularly reflected-gyrating ions. *Journal of Geophysical Research*, 88(A8), 6121–6136. <https://doi.org/10.1029/JA088iA08p06121>
- Scudder, J. D. (1995). A review of the physics of electron heating at collisionless shocks. *Advances in Space Research*, 15(8–9), 181–223. [https://doi.org/10.1016/0273-1177\(94\)00101-6](https://doi.org/10.1016/0273-1177(94)00101-6)
- Shi, Q. Q., Shen, C., Dunlop, M. W., Pu, Z. Y., Zong, Q. G., Liu, Z. X., et al. (2006). Motion of observed structures calculated from multi-point magnetic field measurements: Application to Cluster. *Geophysical Research Letters*, 33(8), L08109. <https://doi.org/10.1029/2005GL025073>
- Shi, Q. Q., Shen, C., Pu, Z. Y., Dunlop, M. W., Zong, Q. G., Zhang, H., et al. (2005). Dimensional analysis of observed structures using multipoint magnetic field measurements: Application to Cluster. *Geophysical Research Letters*, 32(12), L12105. <https://doi.org/10.1029/2005GL022454>
- Vasko, I. Y., Mozer, F. S., Bale, S. D., & Artemyev, A. V. (2022). Ion-acoustic waves in a quasi-perpendicular earth's bow shock. *Geophysical Research Letters*, 49(11), e2022GL098640. <https://doi.org/10.1029/2022GL098640>
- Vasko, I. Y., Mozer, F. S., Krasnoselskikh, V. V., Artemyev, A. V., Agapitov, O. V., Bale, S. D., et al. (2018). Solitary waves across supercritical quasi-perpendicular shocks. *Geophysical Research Letters*, 45(12), 5809–5817. <https://doi.org/10.1029/2018GL077835>
- Vink, J., Broersen, S., Bykov, A., & Gabici, S. (2015). On the electron-ion temperature ratio established by collisionless shocks. *Astronomy & Astrophysics*, 579, A13. <https://doi.org/10.1051/0004-6361/201424612>
- Vogt, J., Haaland, S., & Paschmann, G. (2011). Accuracy of multi-point boundary crossing time analysis. *Annales Geophysicae*, 29(12), 2239–2252. <https://doi.org/10.5194/angeo-29-2239-2011>
- Winske, D., & Quest, K. B. (1988). Magnetic field and density fluctuations at perpendicular supercritical collisionless shocks. *Journal of Geophysical Research*, 93(A9), 9681–9693. <https://doi.org/10.1029/JA093iA09p09681>